POLITECNICO
MILANO 1863

RE.PUBLIC@POLIMI
Research Publications at Politecnico di Milano

Post-Print

This is the accepted version of:

S. Carlotti, F. Maggi
Experimental Techniques for Characterization of Particles in Plumes of Sub-Scale Solid Rocket Motors
Acta Astronautica, Vol. 186, 2021, p. 496-507
doi:10.1016/j.actaastro.2021.06.011

The final publication is available at https://doi.org/10.1016/j.actaastro.2021.06.011

Access to the published version may require subscription.

When citing this work, cite the original published paper.

© 2021. This manuscript version is made available under the CC-BY-NC-ND 4.0 license
http://creativecommons.org/licenses/by-nc-nd/4.0/

Permanent link to this version
http://hdl.handle.net/11311/1180489

Experimental Techniques for Characterization of Particles in Plumes of Sub-Scale Solid Rocket Motors

Stefania Carlotti[a,*], Filippo Maggi[a]

[a] *Politecnico di Milano, Dept. Aerospace Science and Technology, Space Propulsion Laboratory (SPLab-POLIMI), Via La Masa 34, 20156 Milano, Italy*

Abstract

An innovative collection methodology based on a recently developed supersonic probe enabled the collection of alumina particulate from the exhaust plume of a sub-scale solid propellant rocket motor and the comparison with quench collection bomb analysis of propellant incipient agglomeration. Laser diffraction, scanning electron microscopy, and X-ray spectroscopic methods were used to determine particle size, morphology, crystalline nature, and elemental composition. A significant reduction of the particle size occurred across the rocket nozzle. The size distribution resulting from the expansion was monomodal and centred around 2 μm to 3 μm. Propellants containing lower aluminum mass fraction led to number-based distribution in the sub-micrometric region while, for higher metal loading, particle distributions were sensibly shifted towards larger size in the same rocket operative conditions. Similarly, the size was identified to be weakly dependent on chamber pressure, with an increase of the former as the latter decreased. The Hermsen correlation supported and verified the experimental analysis. The majority of the particles was composed by γ-alumina phase, had a typical size lower than 3 μm, and was characterized by smooth surfaces. Occurrences of spitting and collision-to-coalescence phenomena were identified and analyzed.

Keywords: aluminum oxide, particle size distribution, plume, solid rocket motor

*Corresponding author

Email addresses: stefania.carlotti@polimi.it (Stefania Carlotti), filippo.maggi@polimi.it (Filippo Maggi)

Nomenclature

Symbols

$D(3,2)$	Surface mean diameter
$D(4,3)$	Mass mean diameter
$d(0.1)$	10th percentile of the volume-weighted cumulative distribution
$d(0.5)$	50th percentile of the volume-weighted cumulative distribution
$d(0.9)$	90th percentile of the volume-weighted cumulative distribution
d_e	Exit diameter
d_p	Particle diameter
d_t	Throat diameter
ϵ	Expansion ratio
M	Mach number
ξ_c	Aluminum oxide concentration in g-mol/100g
p_c	Combustion chamber pressure
$p_{c_{nom}}$	Nominal combustion chamber pressure
τ	Average chamber residence time

Acronyms

AP	Ammonium Perchlorate
CCP	Condensed Combustion Product
DOA	Dioctyl Adipate
EDX	Energy Dispersive X-ray spectroscpy
EMAP	Experimental Modelling of Alumina Particulate in Solid Boosters
ESA	European Space Agency
FOI	Swedish Defence Research Agency
HTPB	Hydroxyl-Terminated PoliButadiene
P5	Propellant with 5 % of aluminum mass loading
P18	Propellant with 18 % of aluminum mass loading
PSD	Particle Size Distribution
RPC	Rocket Plume Collector
SEM	Scanning Electron Microscope
SOP	Smoke Oxide Particle
SPLab	Space Propulsion Laboratory
SPP	Solid Performance Program
SRB	Solid Rocket Booster
SRM	Solid Rocket Motor
TRP	Basic Technology Research Programme
uAl	Non-agglomerated Aluminum
VMK	Vertikale Messstrecke Köln
XCT	X-ray Computed Tomography
XRD	X-ray Diffraction

1. Introduction

The addition of aluminum to solid propellants improves ideal gravimetric and volumetric specific impulse [1, 2]. However, the presence of aluminum in solid rocket motors (SRMs) greatly complicates the propellant burning process. A fraction of the metal in the propellant tends to aggregate and agglomerate during combustion. Drops of molten

aluminum with an oxide cap leave the burning surface [3, 4] and evolve in the nozzle while they are carried by the gaseous mixture, experiencing a variety of phenomena such as droplet breakup, condensation, evaporation, gas and surface phase reactions [5, 6, 7, 8]. This multiphase flow in SRMs is responsible for specific impulse performance losses [9, 10, 11], enhancement of radiant heat transfer [12], acoustic driving or damping mechanism in the motor cavity [13, 14], impingement and erosion effects on nozzle surfaces [13], slag accumulation in case of submerged configuration [15], rocket plume structure and its signature [16], and involvement in stratospheric ozone depletion [17, 18, 19].

The environmental impact of solid particles suspended in the rocket plume is mostly connected to the heterogeneous reactions triggered by chlorine and leading to reduction of the ozone concentration in the upper layers of the atmosphere. Running processes are similar to those occurring in polar stratospheric clouds [17, 20]. Among them, strong sensitivity was found from chlorine activation reactions which have the potential of doubling the ozone reduction attributed to the emission of solid rocket motors. These chemical processes have been shown to be sensitive to the specific surface area of the particles [18, 19].

The accuracy of plume description, either numerically or experimentally driven, is affected by strong uncertainties. On the one side, reliable modeling prediction is based on the possibility of an adequate code validation on experimental data. On the other hand, the characterization of SRM plumes based on aluminized propellants are featured by intrinsic experimental uncertainty due to aerodynamic particle stratification in the nozzle expansion, high opacity of the flow, conditions of non-equilibrium between the gas and particles, and scattered emission from the nozzle.

This work addresses the need of expanding the knowledge and quantifying the particulate state in proximity of the exit section of a SRM nozzle. Section 2 provides a review of the alumina particles properties in rocket motors and plumes, focusing on their size distribution. Section 3 introduces the propellants and the experimental diagnostics employed in the work, while Section 4 presents and critically discusses the experimental results, comparing them with a theoretical correlation. Section 5 presents a summary of the main conclusions.

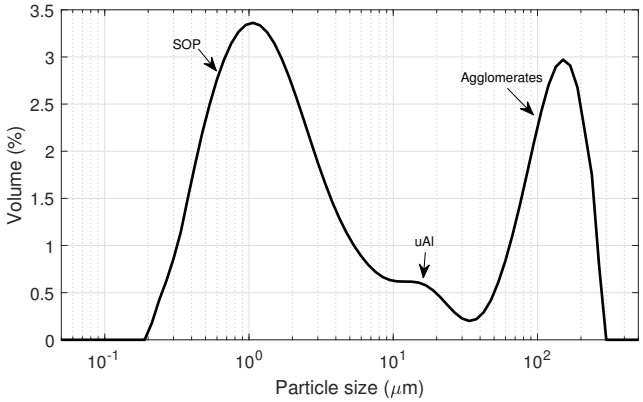

Figure 1: Typical CCP PSD derived from aluminized propellant. Results of the Space Propulsion Laboratory for a metalized propellant containing 14% HTPB, 68 % AP and 18% aluminum, tested at 60 bar.

The experiments addressed in this work were executed in the EMAP (Experimental Modelling of Alumina Particulate in Solid Boosters) framework, an ESA-TRP project pursuing activities concerning the characterization of the condensed particles contained in the exhaust plume of a sub-scale SRM, under different operating conditions. A complete overview of the project and more details about the measurement systems are provided in Saile et al. [21].

2. Background

Several efforts have been made in the past to characterize and/or collect the condensed combustion products (CCPs) in the vicinity of solid propellant burning surface [22, 23, 24, 25, 26, 27]. Analyzing the incipient agglomeration consists of freezing the state of the agglomerates at the instant of release from the combustion surface. Literature data agree on their typical particle size distribution (PSD) at the burning surface and on the parameters having predominant effects on it. An example of a particle size distribution curve for an aluminized propellant is depicted in Fig. 1.

Three main peaks can be distinguished: smoke oxide particles (SOP) are typically found in the lower micro-metric and sub-micrometric region (diameter less than 10 µm) as a result of the gas-phase combustion of non-agglomerated aluminum [28], while ag-

glomerates are distributed in the coarser interval. Depending on the burning conditions, the propellant details, and on the diameter of the virgin original aluminum powder, the peak corresponding to non-agglomerated aluminum (uAl) could be identified as well. The heterogeneous nature of the propellants affects the agglomerations, since the largest oxidizer particles provide fuel rich regions, called pockets, which favor aluminum particles accumulation and aggregation on the burning surface [29, 30]. Hence, agglomerates size increases with aluminum mass fraction and oxidizer size. On the contrary, an increase of the combustion pressure leads to smaller agglomerates, due to lower residence times at the solid-gas combustion interface [31, 32].

After the release, droplets are dragged by the combustion gas products and undergo several transformation processes, each of them affected by uncertain characterization. Coalescence pheonmena may be generated in the convergent part of the nozzle by collision, followed by disgregation in proximity of the throat for shear stress. Alumina solidification and consequent enthalpy release is not deterministic, being influenced by local static temperature, particle thermal inertia, and flow conditions. Particles morphological and physical changes can occur even outside the nozzle, after getting in touch with the external atmosphere due to exhaust plume expansion, interactions with shock waves, afterburning effects, and sudden cooling. All these aspects are influenced by primary propellant and combustion properties (such as aluminum mass loading, residence time, efficiency of the combustion process, combustion chamber pressure, and throat diameters [9, 33]) and by nozzle operating conditions (altitude and nozzle geometry [34]).

The phenomena experienced by the particles/droplets whilst carried through the nozzle by the gaseous mixture significantly modify the chemical and physical properties of alumina. There are little and scattered reported data on the PSD at the exit of a rocket nozzle and within the plume. Attempts to measure the particle size have resulted in a series of technical reports and scientific articles sometimes leading to non-overlapped data and conclusions. In most part, the reason has to be found in a non-uniform approach to the different aspects of metal combustion, producing experimental databases characterized by limited scope. When a global perspective is necessary for validation purposes, data scattering may become critical. Most of the numerical or

modelling activities involving SRM multiphase exhaust flow retrieves particle size distribution data from empirical correlations, theoretical models, or limiting assumptions [33]. All of the prior art on rocket-produced Al_2O_3 particles referred to exhaust from sub-scale rocket motor firings [35, 36, 37, 38, 39, 40], surface or ground cloud collections from Titan [41] and Space Shuttle [34, 42] launches, or measurements and analysis from mid-tropospheric and stratospheric plumes [18, 19, 41, 43].

Measured particle sizes are typically deemed to extend from below 0.25 μm to approximately 13.3 μm [33, 44], and several authors have identified different distributions and main modes. Traineu et al. [36] reported a bimodal distribution in the plume with modes at 3 and 20 μm, while Laredo et al. [35] obtained a quadrimodal distributions with modes at less than 2 μm, 5 μm, 10 μm and 20 μm. According to Gossè et al. [45] particles may range from 0.1 μm to 20 μm, the majority being fine particles with size 0.1 μm to 2 μm. Other researchers have reported particles predominantly or totally in the sub-micrometric range. Dawbarn et al. [39] measured particles in the range 0.1 μm to 4.5 μm, Cofer et al. [43] observed a peak at about 2 μm and another suggested mode at less than 0.3 μm and Schmid et al. [19] stated that 8 % of the total mass of the alumina particles in the plume is in the submicron size range. On the contrary, the studies by Ross et al. have reported that an insignificant percentage of the alumina mass resides in the smallest PSD mode [18]. Moreover, some authors suggested that the fraction of big particles should increment at low altitude and at ground level [46].

Some experimental data and several model predictions indicate a stratification of the particle across the plume, with larger particles concentrated along the plume center line [47, 48]. Hermsen [33] examined several semiempirical correlations and theoretical models for the mass-mean particle diameter D(4,3) in plumes as a function of motor design. According to the author, the main sources of data scattering consisted in the absence of a clear and common test matrix, the difficulty of measuring wide populations of particles, the extreme environmental factors present in rockets, and the existing differences between laboratories and respective analysis techniques. In fact, the mass-weighted D(4,3) data fittings led to deviations sometimes even higher than ± 35 %. Despite the large uncertainties regarding the exact computation on the mean average diameter, the Hermsen correlation was shown to give predicted specific impulses

in good agreement with the experimental values for a number of motors. Equation 1 was mentioned in the AGARD working group report N. 230 [9] and, as suggested by the author, included for use in the Improved Solid Performance Program (SPP) on an interim basis [33]:

$$d_p = 3.6304 d_t^{0.2932}(1 - exp(-0.0008163 \xi_c p_c \tau)) \quad (1)$$

where d_p is the mass-weighted average diameter (μm), d_t (in.) the throat diameter, ξ_c (g-mol/100g) the mole fraction of the condensed phase, p_c (psi) the chamber pressure, and τ (ms) is the average chamber residence time. The standard deviation of this model (s = 0.298) was shown to lead to a deviation in the mass-weighted average diameter of about ± 35%. As originally mentioned by Hermsen, the main dependence on throat diameter is correlated to the velocity gradients in the nozzle, while the term $\xi_c p_c \tau$ is meant to express a limitation on particle size due to growth mechanism in the combustion chamber. It should be noted that the data used for fitting mainly considered rocket motors having high aluminum levels (≥ 15%).

Among the aforementioned studies, some authors focused on the characterization of the crystalline phase of the exhausted CCPs [45, 49]. Particle collection and analysis identified that the aluminum oxide typically present in the exhaust of a solid rocket motor exists in two polymorphic crystal phases: alpha and gamma. The α-alumina is a stable form of the aluminum oxide and it is characterized by a hexagonal structure. On the contrary, the γ-alumina is a transition metastable form, denoted by a complex spinel-like shape [50]. A general agreement could be found regarding the quantification of the crystal phases, as several authors suggested that 60 % to 80 % of the exhaust powder mass is γ-Al_2O_3 [45] and the ratio by mass of gamma to hexagonal alpha phase is four to one, probably driven by the temperature-time history of the particles [49]. In general, experiments indicate that smaller particles tend to be made by gamma phase.

Table 1: Mass composition of the propellants.

	P18, %	**P5, %**
HTPB	14.0	14.0
AP (coarse)	53.3	56.1
AP (fine)	14.2	24.4
μm-Al	18.0	5.0
Fe_2O_3	0.5	0.5

3. Tested Propellants

3.1. Compositions

Two baseline compositions characterized by an aluminum mass fraction of 5 % and 18 % (referred to as P5 and P18, respectively), were provided by the Swedish Defence Research Agency (FOI) to the EMAP project. The propellants were based on conventional ingredients such as ammonium perchlorate (AP) and HTPB as binder. The propellant P5 was used for tuning and validations of some experimental techniques where limited optical thickness was required. The P18 propellant featured a composition similar to the one adopted in Ariane V solid rocket boosters (SRBs). The manufactured grains had end-burning configuration with diameter of 86 mm and length of 107 mm. The two series of propellants have been reproduced on lab-scale at the Space Propulsion Laboratory for further characterization.

The nominal mass compositions are reported in Table 1. Propellants were cured with methylene di-isocyanate, and were plasticized with DOA, containing TEPAN as the bonding agent. A bimodal distribution of AP particle sizes was used for these composite propellants. It contained a mixture of coarse (d(0,5) $\sim$ 70 µm) and fine (d(0,5) $\sim$ 10 µm) particles. The aluminum diameter d(0,5) was 16.5 µm. Nanometric iron(III) oxide (Fe_2O_3) was added as catalyst. Further details on the propellant formulations, ingredients and burning rate tests can be found in Saile et al. [21].

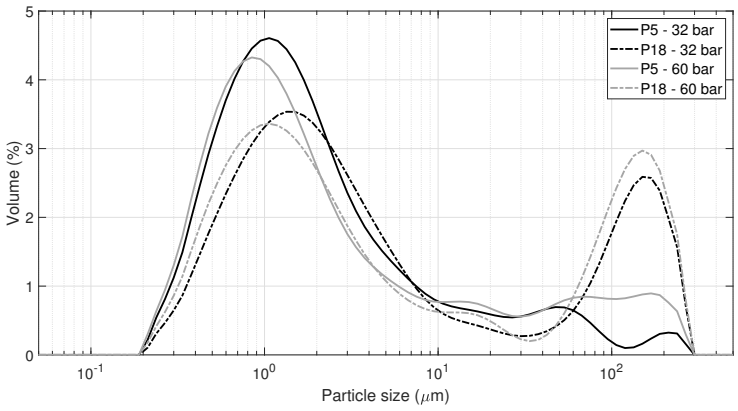

Figure 2: Incipient agglomeration results: particle size distributions for P5 and P18 at different combustion chamber pressure levels

3.1.1. Incipient Agglomeration Tests

Combustion tests were performed in a constant volume chamber by burning propellant strands upside down and quenching the particles released from the propellant surface in a pool filled with quenching liquid few millimeters after the release. Pressure level was kept constant during the test by means of a control loop activating outlet electrovalves. CCPs were finally collected using a pipette and poured into a glass tube. Then, after a washing procedure with acetone and a drying time interval of 48 hours in oven, CCPs were ready to be analyzed.

The average particle size distributions of the collected CCPs are reported in Figure 2, while Table 2 lists the average relevant diameters. Data were obtained through laser diffraction, using Malvern Mastersizer 2000 instrument, equipped with Scirocco (dry) dispersion unit and the proprietary Mastersizer software ver. 5.60 for post-processing [51]. The distribution resulted from the averaging of two different collections. Tests were executed at combustion chamber pressures of interest for the plume particle collection campaign (refer to Section 3.2). The difference between the two pressure levels for both the formulations is not marked, however a shift of the peak at 1 micron towards a sub-micrometric size is observed once the pressure is incremented. Data reported in Table 2 are characterized by large uncertainties related to the measurement

of the coarse fraction, as highlighted by the trend of d(0,9). Hence, the D(4,3) data may not be considered statistically significant due to the coarse mode influence. The absence of a coarse peak for the P5 propellants is caused by the limited fraction of aluminum. The proximity of the particles inside the pocket structure is not enough and the interparticle aggregation cannot occur [30]. On the contrary, the existence of both smoke-oxide particles and agglomerates can be observed for the P18 propellants. High aluminum fraction (18 %) creates the conditions in the pocket for the aggregation-to-agglomeration process. Additionally, a small peak falling in the range of the original aluminum is also visible. It represents the material that was ejected by the propellant without evident agglomeration or combustion. The peak disappears at lower pressure because the residence time in the flame increments and the aluminum has time either to burn in the gas phase or to agglomerate into larger metal drops.

Table 2: CCPs at the burning surface: relevant average volume-weighted mean diameters. Measurement unit is μm.

	d(0, 1)	**d(0, 5)**	**d(0, 9)**	**D(3, 2)**	**D(4, 3)**
P5 - 32 bar	0.474	1.435	18.572	1.057	9.264
P5 - 60 bar	0.449	1.430	64.594	1.042	18.601
P18 - 32 bar	0.598	2.518	153.500	1.527	37.980
P18 - 60 bar	0.532	2.448	161.067	1.403	43.685

3.2. Experimental Setup and Diagnostics

3.2.1. Test Environment

The experiments were executed at the Vertical Test Section in Cologne (VMK). The facility is a blow-down type wind tunnel featuring a vertical and open test section, operating either in subsonic or supersonic flow regime from Mach 0.5 to 3.2 [52, 53]. The setup of the model installed in the wind tunnel mimicked the base region of a space launcher. In the present case, the base region was straight without boat-tailing, directly faced by the nozzle. The experiments were conducted with a subsonic environmental flow at nominal Mach 0.8. The reader should keep in mind that the pressure in the

Table 3: Hot flow tests conditions: nominal pressure levels and corresponding throat diameters; expansion ratios.

$\mathbf{p_c}$**[bar]**	32	60	100
$\mathbf{d_t}$**[mm]**	7.75	6.57	5.74
ϵ	14.4	2.1	1

exterior flow for a wind tunnel with an open test section corresponds to the ambient one. The solid rocket motors were integrated in the base model. Hence, the experiments featured co-flow between the cold ambient flow and hot solid propellant exhaust jet. Three expansion ratios and three chamber pressure levels have been investigated, being the latter controlled by opportunely varying the nozzle throat diameter (refer to Table 3 for further details).

A set of optical and physical diagnostics for the simultaneous characterization of rocket plume was installed downstream the nozzle. A complete overview of the measurement systems, experimental setup, and model geometries is provided in Saile et al. [21], while the present paper focuses on a rocket plume collector, specifically developed for the experiment.

3.2.2. Rocket Plume Collector (RPC)

A rocket plume collector has been used to collect a representative population of particles in the proximity of the nozzle exit section. A simplified scheme is reported in Figure 3. The 5-mm-diameter inlet duct, drilled in a graphite conical nose, captures the incoming supersonic hot flow, which is then slowed and cooled down by a gradual mixing with a secondary inert gas (i.e., nitrogen). After a straight channel ensuring the time and space for complete mixing, the flow enters into a conical divergent channel where the supersonic-to-subsonic transition is expected. The position of the corresponding shock wave is dictated by passively controlled downstream pressure. Finally, a conical liquid spray (i.e., a chlorine-based hydrocarbon liquid), acting in counter-flow with respect to the ingested gas, impacts the particles and the resulting suspension is collected in an annular region. For more information concerning the conceptual and

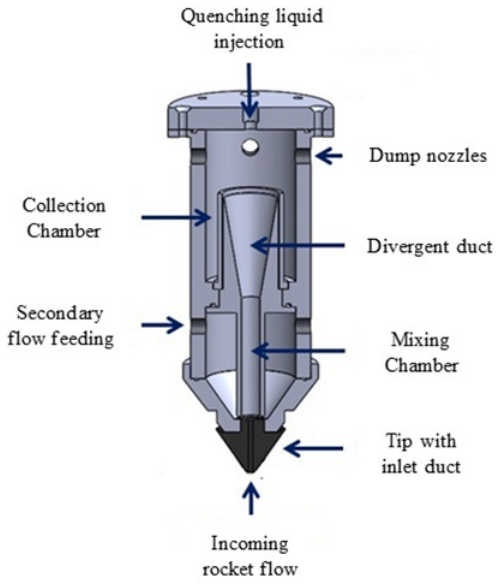

Figure 3: Rocket plume collector operational version.

detailed design of the RPC, the reader is encouraged to refer to Ref. [54], where an in depth discussion on the RPC design drivers can be found. The development of this characterization method targeted the minimal physical and chemical alteration of particles during the collection. Specific care was given to the avoidance of possible bow shocks at the front section, containment of internal shock strength and of velocity gradients generated while the CCPs are still in liquid form, efficient particle cooling and quenching, and reduction of chemical interaction with the secondary environmental flow (post-combustion) as well as with the collection medium.

The robustness of the system was also assessed through numerical sensitivity and uncertainty analysis, discussed in Carlotti et al. [55]. The study demonstrated that most of the effects provoked by uncertainties (pressure levels, mass flow rates, cross sections, possible collection medium evaporation) cancel each other out, resulting in wide operational range. The validation of fluid dynamic and collection concepts has been achieved by means of cold flow experimental tests at the VMK [54]. Explorations of several off-design conditions in relevant environment (i.e., flow at Mach 3 and upstream total pressure ranging from 15 bar to 25 bar) highlighted the correct fluid dynamic be-

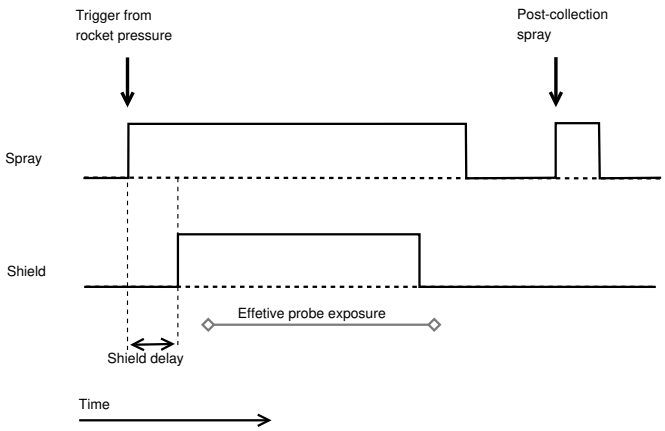

Figure 4: Timing of the experiment during hot flow tests.

haviour and the absence of a bow shock wave in front of the inlet section. The collection methodology was validated seeding the flow with magnesium oxide, capturing the suspended particles with the RPC, and comparing their PSD with the one of the original material.

For the hot flow test campaign, the rocket plume collector was placed at ~ 25 d_e from the nozzle exit due to the free optical patch needed by other non-intrusive techniques of the EMAP consortium. The inlet tip was protected from the exhaust plume by a tungsten thermal shield, operated by a moving arm, commanded by the control loop of the VMK and triggered by the pressure rise at rocket motor ignition. After a pre-determined delay that excluded the initial transient, the quenching spray was triggered, commanding the opening and closure of an electrovalve on the spray feed line. After about 200 ms the opening command was sent to the shield letting the RPC exposed to the rocket plume for 0.5 s. The effective exposure time is influenced by the inertia of the moving arm, but this value is not deemed to be critical for the measurement. A final spray was finally released without inlet flow to clean up the collection volume. The timing of the RPC test is depicted in Figure 4.

The pressure drop across the quenching liquid line was fixed at 12 bar, granting a volumetric flow rate of the collection medium of $2.8\,\mathrm{L\,min^{-1}}$, whereas the mass flow rate of nitrogen for cooling was controlled by a flow meter and set at $27\,\mathrm{g\,s^{-1}}$, achieving

a mass ratio between the secondary and the captured supersonic flows of about 6.5. After each run, internal cleaning and replacement of graphite tip and thermal protections were required to avoid sample contamination.

3.2.3. Post-Processing Diagnostics

Four different diagnostics were used to characterize size, morphology, and composition of the CCPs derived from the experiments. After each collection test, the suspension of particles in quenching medium was extracted from the probe. Separation between solid and liquid phase was obtained by means of centrifuge cycles at 2500 rpm. At the end of each run, the quenching liquid was removed and the remaining precipitate was washed using a ketone solvent. Finally, oven drying ensured the preservation of the collected material during transportation. When required by post-test analysis, particles were re-suspended in 10 mL of solvent with ultrasound treatment to assure their dispersion.

Particle size distribution was evaluated by laser diffraction, using Malvern Mastersizer 2000 with wet dispersion (Hydro, 2000S) [51]. Special care is required due to dispersion issues when the typical powder dimension falls below the micrometric range. The pre-treated sample was further dispersed in bi-distillated water using octylphenoxypolyethoxyethanol additive, a non-ionic surfactant which commercial name is Igepal CA-630. Obscuration levels (i.e., the amount of light scattered by the particles, that is commonly used as a measure of their concentration) were monitored. Tests with obscuration value lower than 0.3 were discarded from the analysis. The same sample was measured multiple times until a minimum of three reproducible measurements was achieved. The proprietary Mastersizer software ver. 5.60 for post-processing [51] was used for average values computation. In the data reduction approach, spherical and smooth-texture particles were assumed. Mass-mean diameter D(4,3), surface-mean diameter D(3,2), span of the distribution, and volume-, and number-based particle size distributions could be evaluated.

Particle morphology was obtained through scanning electron microscopy (SEM). The images were obtained by a Hitachi TM 3000 scanning electron microscope at 15 kV and several magnifications. Each pre-treated sample was laid on a metal support provided with a conductive graphite-based bi-adhesive tape and mounted on a multi-

sample holder. Images could be taken after the solvent was evaporated. In addition, the particle diameters were qualitatively derived to cross check the results obtained with the laser diffraction methodology.

The presence of crystalline phases and the relative percentage were obtained through X-ray diffraction (XRD). Analyses were executed by a PANalytical X'Pert alpha-1 $\Theta/2\Theta$ X-ray diffractometer with Bragg-Brentano geometry. Preparation consisted in positioning and leveling a small amount of powder inside a zero-background sample holder. Powder was not pre-treated. Tests were executed using a radiation X Cu K_α (λ = 1.5416 Å) at 1.6 kW. The selected angular range was 5° to 90° (2Θ) with a pass of 0.02° (2Θ) and an acquisition time of 15 s per pass. Search of identified inorganic phase was performed using the Hanawal method. Phase composition, residual strain (macrostrain), crystal structure, size, and micro-strain can be recognized and quantified if possible.

The energy dispersive X-ray spectroscopy (EDX) was used for elemental analysis or chemical characterization of a sample and to estimate the relative percentage of the identified chemical elements. Tests were executed by a Jeol JSM -7600F microscope, equipped with two detectors for secondary electrons and two detectors for backscattered electrons, coupled with an energy dispersion X-ray spectrometer. Carbon was used as background material. The reader should be aware that a deconvoluted elemental analysis was not performed.

3.3. Test Matrix

Twelve collection tests on aluminized propellants have been executed. The summary of the investigated conditions is depicted in Table 4. Pressure levels, nozzle configurations and aluminum loadings, along with post-processing techniques and eventual comments on the outcome of the experimental test outcomes, are listed. The first two tests of the experimental campaign (i.e., RPC1 and RPC2) have been unsuccessful because of the graphite tip failure due to its incorrect installation. Among the other tests, four of them (RPC3, RPC4, RPC8 and RPC11) collected insufficient material for laser diffraction analysis, thus information on the particles size have been qualitatively obtained by SEM observations.

Table 4: RPC runs: summary of investigated conditions.

	Firing Conditions			**Post-Processing Techniques**			
Run-Id	$\mathbf{p_{c_{nom}}}$ [bar]	ϵ	**Loading**	PSD	SEM	XRD	EDX
RPC1*	32	14.4	5% Al				
RPC2*	32	1	5% Al				
RPC3	32	2.1	5% Al		X		
RPC4	32	14.4	5% Al		X		
RPC5	60	1	5% Al	X	X	X	X
RPC6	60	14.4	5% Al	X	X	X	X
RPC7	32	1	18% Al	X	X	X	X
RPC8**	32	14.4	18% Al		X	X	X
RPC9	60	1	18% Al	X	X	X	X
RPC10	60	14.4	18% Al	X	X	X	X
RPC11**	32	2.1	18% Al		X	X	
RPC12	100	14.4	18% Al	X	X	X	X

$*$ Failure of the tip

$**$ Low amount of collected material

4. Results and Discussion

4.1. Physical Characterization

Volume and number-based particle size distributions, as well as average relevant diameters are shown in Fig. 5 and tabulated in Table 5. For the sake of completeness, obscuration values are included. The experimental campaign was enough to give indications on trends and lead to preliminary considerations, despite the limited number of planned tests did not permit statistical treatment of data.

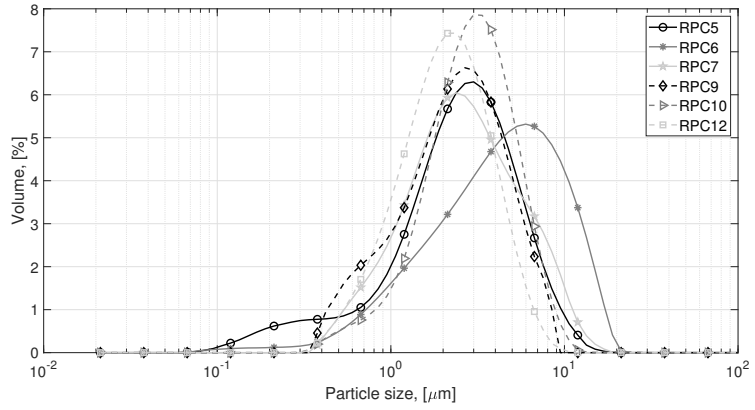

(a)

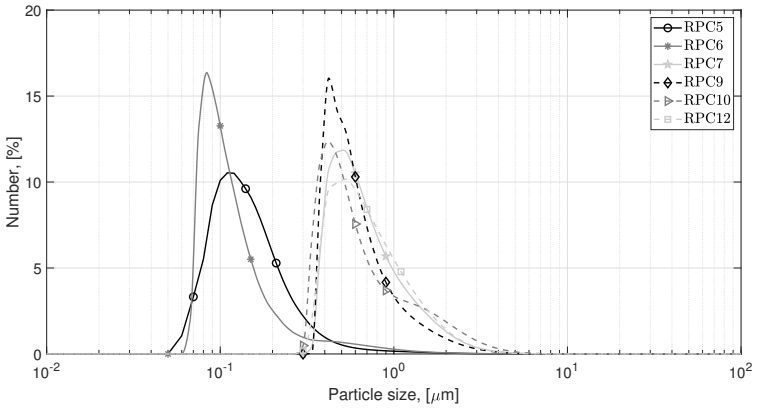

(b)

Figure 5: CCPs collection in plume: comparison of (a) volume-weighted particle size distribution; (b) number-weighted particle size distribution.

Table 5: Average volume-weighted relevant diameters (in μm). Data reduction performed with Mastersizer 2000 software ver. 5.60 [51]. For clarity, firing conditions for each run are reported.

Id.	$\mathbf{p_{c_{nom}}}$ [bar]	ϵ	**Loading**	**d(0.1)**	**d(0.5)**	**d(0.9)**	**Span***	**D(4, 3)**	**D(3, 2)**	Obscuration
RPC5	60	1	5% Al	0.637	2.551	6.015	2.108	3.050	1.287	0.58
RPC6	60	14.4	5% Al	1.105	4.364	11.09	2.287	5.321	2.214	0.66
RPC7	32	1	18% Al	0.938	2.555	6.981	2.365	3.344	1.933	0.58
RPC9	60	1	18% Al	0.781	2.370	5.261	1.890	2.743	1.900	0.33
RPC10	60	14.4	18% Al	1.250	2.930	5.827	1.562	3.299	2.251	6.19
RPC12	100	14.4	18% Al	0.884	2.083	4.322	1.651	2.395	1.665	0.77

*: Span = $\frac{d(0.9)-d(0.1)}{d(0.5)}$

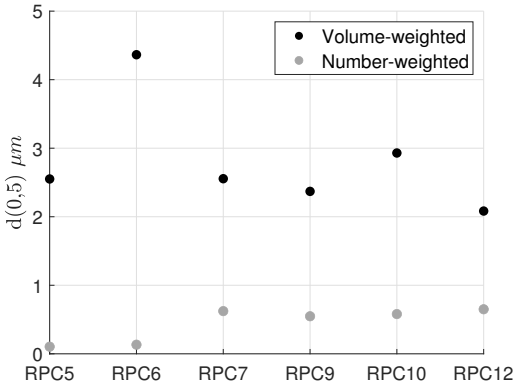

Figure 6: CCPs collection in plume: comparison of average volume-weighted and average number-weighted d(0,5).

A general agreement between the PSDs regardless the rocket motor conditions is evident in Fig. 5a. A single mode can be identified for all the distributions, featuring an average peak around 2 μm to 3 μm. Exceptions are the RPC6 run, which is slightly shifted towards higher values (i.e., d(0.5) ≈ 4 μm) and runs RPC5 and RPC9 which feature a small mode in the sub-micron range. The span for all the collections ranges between 1.5 μm to 2.5 μm, documenting the production of narrow particle size distributions. Generally speaking, the computation of D(4,3) overweights the presence of larger particles when compared to D(3,2) and to number-based average. Thus, the similarity of the mean diameter (d(0.5)) and the other weighted diameters (D(4,3) and

D(3,2)) confirm the tight range of the populations. More meticulous observations on Table 5 suggest the presence of larger particles in RPC5 and RPC6 tests, being D(4,3) more than doubled with respect to D(3,2). For RPC5 the cumulative size distribution, represented by d(0.1), d(0.5), and d(0.9), is still in line with the other tests suggesting the presence of few occasional larger collected items. The small values of the D(3,2) and of the number weighted diameter identify the presence of a fine population. Rather, the cumulative distribution produced by the RPC6 test is slightly shifted towards larger values.

The number-based particle size distributions are depicted in Fig. 5b. Similar trends can be identified, with some distinctive differences, though. The number-based distributions generated by the 5 % Al-loaded propellant are almost overlapped, despite they were obtained in different conditions. The peak is centred around 100 nm. The same consideration can be done for the 18 % Al-loaded propellants, although curves are shifted towards higher values and the peak is found at 400 nm).

If the comparison is done with the volume and number based distributions of the incipient agglomeration (see Fig. 2), shape similarity with the exhausted particles seems to be lost, highlighting the effects of break-up processes on large agglomerates when passing through the nozzle. The P18 propellant exhibits a pronounced peak in the coarse region (c.a. 100 μm). On the contrary, the P5 is characterized by a contained coarse mode. After nozzle exhaust, the complete disappearance of the coarse peak and the shift towards lower size for the PSD can be appreciated in Fig. 5a. Nevertheless, it can be observed that the difference between the peak values of the number based distributions are correlated to the metal loading fraction as they are systematically larger for the propellant P18. An explanation may be based on the incremented concentration of aluminum oxide fine and ultrafine droplets in presence of a higher original metal loading. These smoke-kind particles, still liquid under combustion chamber conditions, are suspended in the gas phase and may merge each other after reciprocal collision. This event is less probable for lower propellant metal content.

A weak dependence on the combustion chamber pressure can also be identified. The reader should keep in mind that the pressure was tuned by varying the throat diameter. Hence, the following results emphasize also the dependence of particles on

d_t, in turn correlated to the velocity gradients in the nozzle. Results suggest that the increase of the combustion chamber pressure (i.e., the decrease of the throat diameter) produces a slight decrease of the particle sizes, as visible in results for RPC7 compared to RPC9 and RPC10 compared to RPC12. However, other effects may be involved in the process. Higher combustion chamber pressure may lead to more fragmentation because of higher aerodynamic forces on the droplets. Also, as suggested in literature, incipient agglomeration is favorably influenced by pressure because agglomerates resulting from propellant combustion are smaller. This is a consequence of the reduced residence time of metal powder at the burning surface when pressure and, thus, burning rate is incremented.

Similarly, a dependence on the expansion ratio can be identified, with an increase of the volume-based diameter as the expansion ratio increases. Referring to Table 5, results concerning runs RPC5 vs RPC6 and RPC9 vs RPC10 support this consideration. Several possible explanations for this result may be taken into account. In particular, particle collision on the nozzle wall divergent section may lead to the formation of a wall film. Its destabilization by the flow may lead to the detachment of large flakes/drops. Several factors influence the flow of deposited liquid metal along the walls. Among the others, particles size and streamlines, expansion ratio and nozzle contour of the divergent part can play an active role. Without any aim of generalities, the present discussion will focus only on the influence of the divergent part as a function of the expansion ratios tested during the experimental campaign. Hints supporting its influence were found by post-fire collection of solidified metal deposits on the divergent part of the nozzle [21], as shown in Fig. 7a. Their non-uniform shape, resulting from X-ray computed tomographic (XCT) analysis, supported this interpretation (refer to Fig. 7b [56]). Consequently, entrained flakes/drops may be subjected to concurrent break up and collision processes in the main flow. Further investigations are needed to derive more precise conclusions.

(a)

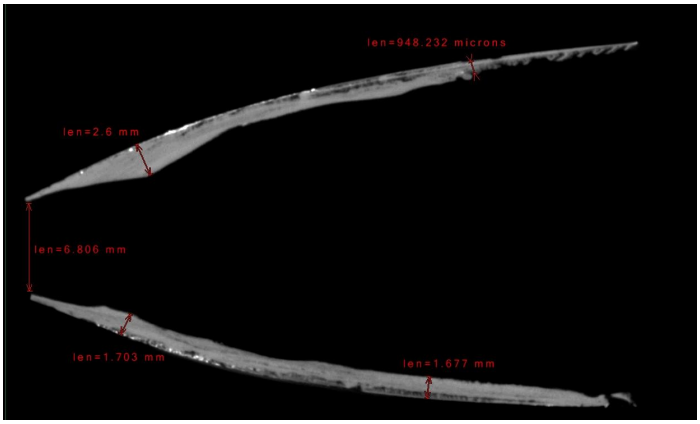

(b)

Figure 7: (a) Example of nozzle deposition in the divergent; (b) Axial cut from XCT reconstruction

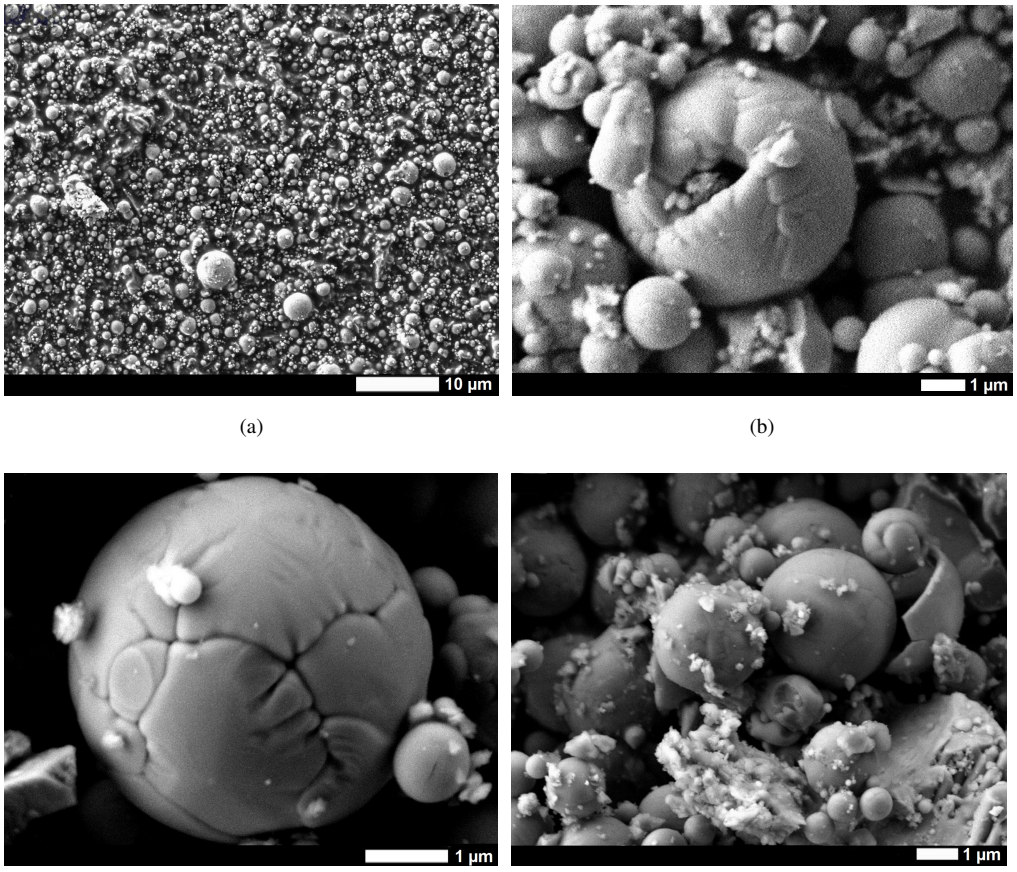

(a) (b)

(c) (d)

Figure 8: SEM images: (a) example of spherical particles ensemble, RPC10 ($p_{c_{nom}}$ = 60 bar, ϵ = 14.4, 18% Al); magnification of hollow, fractured and broken particles: (b) RPC7 ($p_{c_{nom}}$ = 32 bar, ϵ = 1, 18% Al), (c)-(d) RPC9 ($p_{c_{nom}}$ = 60 bar, ϵ = 1, 18% Al).

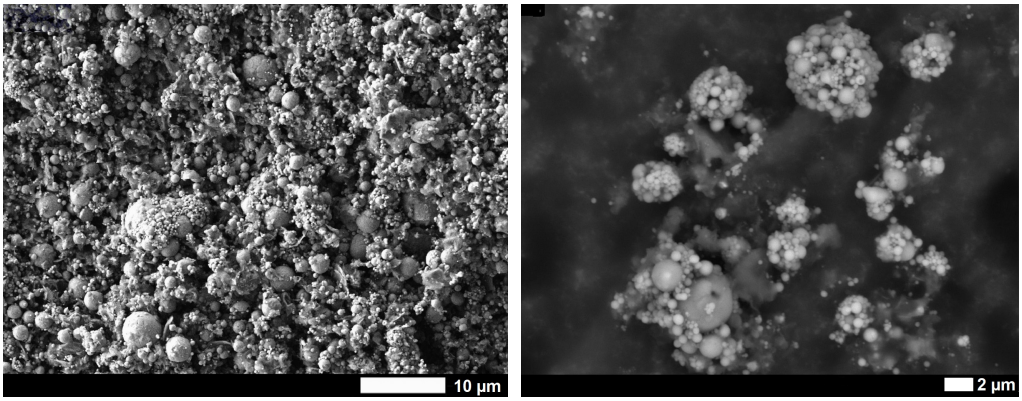

(a) (b)

(c)

Figure 9: SEM images: example of particles with sintered surfaces: RPC6 ($p_{c_{nom}}$ = 60 bar, ϵ = 14.4, 5% Al) (a) global view and (b) magnification of single particles/clusters; (c) example of flakes, RPC5 ($p_{c_{nom}}$ = 60 bar, ϵ = 1, 5% Al).

SEM observations for each test listed in Table 4 confirm the particle size results obtained with laser diffraction. Particles are mainly spherical (see Fig. 8a) and range from 0.1 μm to 6 μm in diameter, the large majority being fine ones, between 0.1 μm to 2 μm.

SEM images are presented in Figures 8 and 9. The smoothness of particle surfaces typically observed in these collections seems to indicate low porosity. Systematic occurrences of large fractured hollow particles (larger than 2 μm) were detected regardless the motor operating conditions (see Figs. 8b, 8c, and 8d). This process is deemed to occur because of the outwards non-uniform diffusion of liquid aluminum and of the entrapped gas through the alumina shell. This phenomenon is known in the literature as spitting [45]. In this process the surplus of water vapor is expelled from the particles during solidification (typically at the exit of the nozzle), near alumina melting temperature (2327 K). Cracks or holes suggest that particles may be hollow. In fact, liquid alumina is able to dissolve gaseous H_2O which diffuses outwards forming an internal cavity. An example of broken hollow particle is shown in Fig.8b.

In contrast to the systematic detection of hollow particles with unique shell, particles with several surface features was detected. The sintered surface aspect is presumably the results of incomplete collision-to-coalescence processes of many molten alumina particles in the exhaust plume. However, considering the different conditions in terms of rocket parameters among these three runs, the definition of a common physical process justifying this behavior is not straightforward.

4.2. Chemical Characterization

A typical X-ray diffraction pattern is reported in Fig. 10. The black curve reports on the vertical axis the intensity of diffracted signal as a function of the different angles (horizontal axis). The symbols show the ideal pattern of the crystalline structures identified by the software.

X-ray diffraction results are listed in Table 6. The absence of metallic (crystalline) aluminum in the collected powder demonstrates that the residence time in the combustion chamber was enough to grant complete metal oxidation, enabling its full enthalpy release. According to the literature about particles in plume collection [44][45], drops

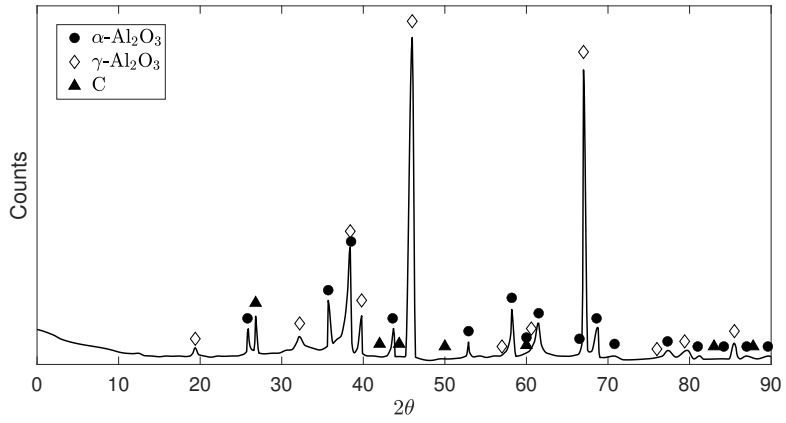

Figure 10: Example of XRD outcomes: identification of $\gamma - Al_2O_3$, $\alpha - Al_2O_3$ and Graphite. Results for RPC12 ($p_{c_{nom}}$ = 100 bar, ϵ = 14.4, 18% Al).

smaller than 3 µm in diameter do not contain α-Al_2O_3, providing a cross-check of the results obtained from laser diffraction and SEM. However, some exceptions may be identified. Run RPC9 shows percentage of γ-Al_2O_3 and α-Al_2O_3 almost comparable, while runs RPC8 and RPC11 feature an opposite trend. It must be noted that a small amount of powder was available for these analysis. A significant point there was no residual unreacted (crystalline) aluminum in the collected powder the absence of metallic aluminum demonstrates that residence time in the combustion chamber was enough to grant complete metal oxidation, enabling its full enthalpy release. Minor traces of graphite have been identified in some of the tests. The low percentage suggests that the erosion of the graphite tip, if occurred, did not influence the final measurement accuracy. Additionally, contaminations of silicon oxide (thermal protection), Fe^0 (combustion chamber and nozzle structures), and $CaCO_3$ (surrounding environment) have been measured in small amount.

The energy dispersive X-ray spectroscopy results are listed in Table 7. Oxygen and aluminum resulted the main elements of the collected sample. According to the chemical formula of alumina, the relative percentage of aluminum and oxygen in the aluminum oxide should be 40 % and 60 %, respectively. The comparable atomic fraction of Al and O suggests the existence of metal sub-oxides or even aluminum in amorphous

Table 6: XRD Results: recognized phase and quantitative analysis in mass percent.

Id.	$\gamma - Al_2O_3$	$\alpha - Al_2O_3$	Graphite	SiO_2	$CaCO_3$	Si^0	Fe^0
RPC4	85.6	-	0.1	-	-	-	14.3
RPC5	95.8	-	3.3	-	-	0.9	-
RPC6	92.2	2.9	4.9	-	-	-	-
RPC7	84.2	5.6	-	8.7	1.1	0.4	-
RPC8*	35.3	64.5	0.2	-	-	-	-
RPC9	58.4	40.4	-	-	0.6	0.6	-
RPC10	84.7	14.4	0.9	-	-	-	-
RPC11*	36.8	57.7	-	-	5.5	-	-
RPC12	86.7	9.7	3.6	-	-	-	-

*: Low amount of original powder

state, as they were not detected by the XRD analysis. EDX observations confirm also the existence of contaminants from nozzle and/or chamber case (i.e., Ni/Fe/Cr), and from thermal protections (i.e., Si), although in minor extent. Finally, a small and persistent Cl signal was observed on most samples but it cannot be determined whether it was bonded to the particles, or adsorbed or chemisorbed on the surfaces. Thus, it is not possible to discriminate whether the chlorine is a sign of combustion and afterburning processes, or it is a residue of the analysis procedure.

4.3. Data Comparison with Literature and Relevant Correlation

The increase of the particles average diameter with the condensed phase mole fraction is supported by theoretical considerations regarding SRMs internal combustion and fluid dynamics. In fact, the heterogeneous nature of the propellants affects the agglomeration, since incipient agglomerate size increases with aluminum mass fraction. Similarly, the concentration of aluminum oxide fine and ultrafine droplets increases in presence of a higher original metal loading. These smoke-kind particles, still liquid under combustion chamber conditions, are suspended in the gas phase and may merge each other after reciprocal collision. This event is less probable for lower propellant

Table 7: EDX Results: elemental percentages.

Id.	$\%O$	$\%Al$	$\%Ni/Fe/Cr$	$\%Si$	$\%Cl$	$\%Others$
RPC4	57.6	36.8	4.1	1.0	0.5	0.0
RPC5	46.4	44.7	4.5	2.4	1.0	1.0
RPC6	48.6	48.0	0.9	1.0	1.0	0.5
RPC7	48.3	43.1	5.2	1.4	1.6	0.8
RPC8	53.9	44.3	0.9	0.7	0.2	0.0
RPC9	50.0	43.9	2.5	3.7	0.2	0.6
RPC10	51.1	47.4	0.9	0.3	0.1	0.2
RPC12	55.1	43.6	0.8	0.3	0.1	0.1

metal content. This consideration emphasizes the importance of the particulate number density in the chamber and in the nozzle, being the particles involved also in the collision processes leading to coalescence (i.e., particularly in the convergent part of the nozzle), as suggested by literature [57].

The increment of CCPs from P5 to P18 is verified by ideal thermochemical computations performed through NASA CEA code [58]. The analysis aims at quantifying the mass and mole fractions of alumina at the nozzle exit and is performed on the same AP/Al/HTPB propellant compositions used in the experimental tests, and on the nominal operating conditions. Shifting equilibrium expansion model (i.e., infinite reaction rate [59]) is adopted. The reader should be aware that thermochemistry cannot predict the size of the agglomerates. The mass reported in Table 8 is the total CCP amount, throughout the entire PSD. The results clearly show that the sole change of equilibrium chemistry due to pressure variations cannot be responsible of CCP amount variation while original metal loading is. The particle size is bonded also to the complex physics of the combustion/expansion process.

Several correlations are available in the open literature to describe the relation between diameters of particles exiting from the nozzle and relevant rocket parameters. The Hermsen correlation (see Eq. 1) [33] is recalled, for a verification of the experimentally derived PSDs.

Table 8: Thermochemical computation results: comparison of alumina fractions at different aluminum loadings.

Pressure, bar	Propellant	CCP concentration, g/100g	ξ_c, g-mol/100g
32	P5	9.31	0.0913
	P18	31.85	0.3124
60	P5	9.28	0.0910
	P18	31.94	0.3133

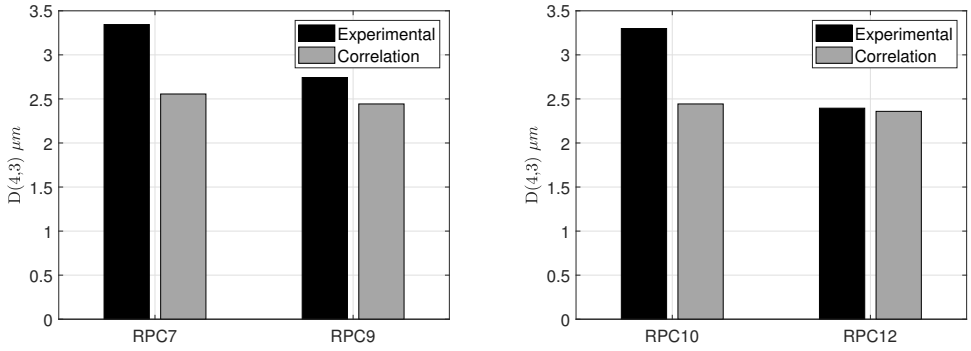

(a) (b)

Figure 11: D(4,3) comparison between experimental results and Hermsen correlation: (a) tests at ϵ = 1 and 18% Al. Comparison between $p_{c_{nom}}$ = 32 bar (RPC7) and $p_{c_{nom}}$ = 60 bar (RPC9); (b) tests at ϵ = 14.4 and 18% Al. Comparison between $p_{c_{nom}}$ = 60 bar (RPC10) and $p_{c_{nom}}$ = 100 bar (RPC12).

Figure 11 compares the mass-weighted average diameters computed according to Eq. 1 to the experimentally-derived ones. The results were obtained by considering the aluminum concentrations tabulated in Table 8, the nominal values for chamber pressures (and corresponding throat diameters), and τ = 50 ms [10]. The global size range is correctly captured, highlighting the validity of the experimental diagnostics and post-processing techniques. The coupled influence of chamber pressure and throat diameter is appreciable. Despite the difference in the absolute values is less marked for the Hermsen correlation, the trend observed by the experimental campaign is confirmed.

5. Conclusion

This work has presented a programmatic experimental activity for alumina characterization in the exhaust plume. Particle size distribution, morphology, crystal phase, and elemental composition have been analyzed. Twelve tests were executed at several combustion chamber pressure, expansion ratio, and aluminum loading to verify the influence of these parameters on the particulate. Ten out of twelve tests led to successful particle collection by means of an innovative intrusive technique merging the concept of high-temperature supersonic probe and particle quenching. Collected materials were post processed by means of laser diffraction with water dispersion, SEM, XRD, and EDX techniques.

Even though single tests for each aforementioned configuration were executed, a general agreement in terms of volume mean diameter, Sauter diameter, and volume weighted diameters was identified. Comparison between single runs has shown possible influence of pressure, aluminum loading, and expansion ratio.

A single mode has been identified for all the particle size distribution, featuring a peak around 2 μm to 3 μm, and a D(4,3) in the range 2.3 μm to 5 μm. Propellants with lower aluminum mass fraction have generated number-based distributions in the sub-micrometric region sensibly shifted towards smaller size with respect to those containing higher metal loads, in the same rocket operative conditions. This experimental result was verified against theoretical considerations and thermophysical computations. Similarly, a slight dependency on pressure, tuned by the throat diameter, was identified. This consideration was supported by the comparison between the experimental results and the $D(4,3)$ computed according to Hermsen correlation. It is worth underlining the agreement between the empirical fitting and the experimental results on the global particle size range. SEM images confirmed that the large majority of the collected particles are in the sub-micrometric range, with some minor occurrences not larger than 6 μm. Morphology was quite variable, ranging from spherical large hollow particles, caused by the spitting phenomena, to aggregates of ultrafine particles. Most of the runs showed percentages of the alumina crystal phase in good agreement with the literature. The majority of it tended to be of the γ-phase, which is typical of the smallest exhaust

particles. The elemental analysis added some information on the chemical composition. Both techniques were able to identify minor traces of contaminant from hardware erosion and from the environment.

The presented results expand the knowledge of the particulate state at the exit section of the nozzle, from a quantitative view point. Moreover, a complete programmatic framework of techniques was assessed, capable of reliably characterizing properties of the solid rocket exhaust particulate and comparing it with the original incipient agglomeration. Results were consistent with existing literature data, and were verified. The experimental campaign was enough to give preliminary indications on trends, despite multiple tests under the same operating conditions should be foreseen for statistical data treatment in future experimental campaign. Clearly, the limited amount of collected material was the most critical aspect of the experimental campaign, causing potential risk of low reproducibility. This last aspect can be overcome when up-scaling the collection methodology for future experimental programs with larger rocket motors.

Acknowledgments

The authors acknowledge the financial support of the ESA-funded research activity EMAP (Experimental Modelling of Alumina Particulate in Solid Booster), ESA contract No. 4000114698/15/NL/SFe. The authors wish to recognize and acknowledge the significant contribution of Dr. Gianluigi Marra of the Research Center for Non Conventional Energy, Eni Donegani Institute (Novara, Italy).

References

[1] L. T. De Luca, L. Galfetti, F. Maggi, G. Colombo, A. Reina, S. Dossi, D. Consonni, M. Brambilla, Innovative metallized formulations for solid or hybrid rocket propulsion, Chinese Journal Energetic Materials 20 (4) (2012) pp. 465–474. doi:10.3969/j.issn.1006-9941.2012.04.018.

[2] N. Kubota, Propellants and Explosives: Thermochemical Aapects of Combustion, Chapter 4, 3rd Edition, Wiley-VCH Verlag GmbH, Weinheim, 2015.

[3] E. W. Price, Combustion of metallized propellants, in: AIAA Progress in Astronautics and Aeronautics, Vol. 90: Fundamentals of Solid Propellant Combustion, AIAA, New York, 1984, pp. 478–513.

[4] L. DeLuca, L. Galfetti, G. Colombo, F. Maggi, A. Bandera, V. A. Babuk, V. P. Sinditskii, Microstructure effects in aluminized solid rocket propellants, Journal of Propulsion and Power 26 (4) (2010) pp. 724–733. doi:10.2514/1.45262.

[5] S. Carlotti, J. Anfossi, R. Bellini, G. Colombo, F. Maggi, Particulate phase evolution inside solid rocket motors: Preliminary results, in: 8th European Conference for Aerospace Sciences (EUCASS 2019), 2019, pp. 1–13. doi:10.13009/EUCASS2019-787.

[6] L. H. Caveny, A. Gany, Breakup of Al/Al2O3 agglomerates in accelerating flowfields, AIAA Journal 17 (12) (1979) pp. 1368–1371. doi:10.2514/3.7633.

[7] J. C. Melcher, R. L. Burton, H. Krier, Combustion of aluminum particles in solid rocket motor flows, AIAA Paper No. 99-2630 (1999). doi:10.2514/6.1999-2630.

[8] J. C. Melcher, H. Krier, R. L. Burton, Burning aluminum particles inside a laboratory-scale solid rocket motor, Journal of Propulsion and Power 18 (3) (2002) pp. 631–640. doi:10.2514/2.5977.

[9] D. Reydellet, Performance of rocket motors with metallized propellants (AGARD PEP WG-17), AGARD Advisory Report AR-230 (1986).

[10] W. H. Miller, Solid rocket motor performance analysis and prediction, NASA Techical Report No. NASA-SP-8039 (1971).

[11] F. Maggi, A. Bandera, L. Galfetti, L. T. DeLuca, T. L. Jackson, Efficient solid rocket propulsion for access to space, Acta Astronautica 66 (11-12) (2010) pp. 1563–1573. doi:10.1016/j.actaastro.2009.10.012.

[12] J. Harrison, M. Q. Brewster, Analysis of thermal radiation from burning aluminium in solid propellants, Combustion Theory and Modeling 13 (3) (2009) pp. 389–411. doi:10.1080/13647830802684318.

[13] J. Dupays, Y. Fabignon, P. Villedieu, G. Lavergne, J. Estivalezes, Some aspects of two-phase flows in solid-propellant rocket motors, in: Solid Propellant Chemistry, Combustion, and Motor Interior Ballistics, Progress in Astronautics and Aeronautics, Vol. 185, AIAA, 2000, pp. 859–883. doi:10.2514/5.9781600866562.0859.0883.

[14] S. Gallier, F. Godfroy, Aluminum combustion driven instabilities in solid rocket motors, Journal of Propulsion and Power 25 (2) (2009) pp. 509–521. doi:10.2514/1.37664.

[15] B. Tóth, M. R. Lema, P. Rambaud, J. Anthoine, Assessment of slag accumulation in solid rocket boosters: summary of the VKI research, AIAA Paper No. 2007-5760 (2007). doi:10.2514/6.2007-5760.

[16] S. M. Dash, B. E. Pearce, H. S. Pergament, E. S. Fishburne, Prediction of rocket plume flowfields for infrared signature studies, Journal of Spacecraft and Rockets 17 (3) (1980) pp. 190–199. doi:10.2514/3.28030.

[17] R. C. Sullivan, T. Thornberry, J. P. D. Abbatt, Ozone decomposition kinetics on alumina: effects of ozone partial pressure, relative humidity and repeated oxidation cycles, Atmospheric Chemistry and Physics, European Geosciences Union 4 (5) (2004) pp. 1301–1310, HAL Id : hal-00295482.

[18] M. N. Ross, P. D. Whitefield, D. E. Hagen, A. R. Hopkins, In situ measurement of the aerosol size distribution in stratospheric solid rocket motor exhaust plumes, Geophysical Research Letters 26 (7) (1999) pp. 819–822. doi:10.1029/1999GL900085.

[19] O. Schmid, J. M. Reeves, J. C. Wilson, C. Wiedinmyer, C. A. Brock, D. W. Toohey, L. M. Avallone, A. M. Gates, M. N. Ross, Size-resolved particle emission indices in the stratospheric plume of an Athena II rocket, Journal of Geophysical Research: Atmospheres 108 (D8) (2003) pp. 4250–56. doi:10.1029/2002JD002486.

[20] S. Solomon, The mystery of the Antarctic ozone "Hole", Reviews of Geophysics, 26 (1) (1988) pp. 131–148. doi:10.1029/RG026i001p00131.

[21] D. Saile, D. Allofs, V. Kühl, L. Steffens, A. Gülhan, M. Beversdorff, W. Förste, C. Willert, S. Carlotti, L. M. Maggi, Filippo, N. Wingborg, T. Langener, J. van den Eynde, Characterization of SRM plumes with alumina particulate in subscale testing, CEAS Space Journal (2020). doi:10.1007/s12567-020-00338-0.

[22] R. W. Devillers, G. Le Besnerais, M. Nugue, N. Cesco, Experimental analysis of solid-propellant surface during combustion with shadowgraphy images: new tools to assist aluminum-agglomeration modelling, in: 7th European Conference for Aeronautics and Space Sciences (EUCASS), EUCASS Paper 2017-327, 2017, Milan, Italy. doi:10.13009/EUCASS2017-327.

[23] M. S. Powell, I. W. Gunduz, W. Shang, J. Chen, S. F. Son, Y. Chen, D. R. Guildenbecher, Agglomerate sizing in aluminized propellants using digital inline holography and traditional diagnostics, Journal of Propulsion and Power 34 (4) (2018) pp. 1002–1014. doi:10.2514/1.B36859.

[24] S. Gallier, J.-G. Kratz, N. Quaglia, G. Fouin, Detailed analysis of a quench bomb for the study of aluminum agglomeration in solid propellants, in: Progress in Propulsion Physics, Vol. 8, EDP Sciences, 2016, pp. 197–212. doi:10.1051/eucass/201608197.

[25] J. Hijlkema, P. Prévot, M. Prevost, V. Mironov, Particle size distribution measurements in the Keldysh Research Centre experimental setup at ONERA, AIAA Paper No. 2011-5712 (2011). doi:10.2514/6.2011-5712.

[26] F. Maggi, A. Bandera, L. T. De Luca, V. Thoorens, J. F. Trubert, T. L. Jackson, Agglomeration in solid rocket propellants: novel experimental and modeling methods, in: Progress in Propulsion Physics, Vol. 2, EDP Sciences, 2011, pp. 81–98. doi:10.1051/eucass/201102081.

[27] T.-K. Liu, Experimental and model study of agglomeration of burning aluminized

propellants, Journal of Propulsion and Power 21 (5) (2005) pp. 797–806. doi:10.2514/1.11988.

[28] V. A. Babuk, Problems in studying formation of smoke oxide particles in combustion of aluminized solid propellants, Combustion, Explosion, and Shock Waves 43 (1) (2007) pp. 38–45. doi:10.1007/s10573-007-0006-5.

[29] N. S. Cohen, A pocket model for aluminum agglomeration in composite propellants, AIAA Journal 21 (5) (1983) pp. 720–725. doi:10.2514/3.8139.

[30] F. Maggi, L. T. DeLuca, A. Bandera, Pocket model for Aluminum agglomeration based on propellant microstructure, AIAA Journal 53 (11) (2015) pp. 3395–3403. doi:10.2514/1.j053992.

[31] V. A. Babuk, V. A. Vasilyev, M. S. Malakhov, Condensed combustion products at the burning surface of aluminized solid propellant, Journal of Propulsion and Power 15 (6) (1999) pp. 783–793. doi:10.2514/2.5497.

[32] F. Maggi, S. Dossi, C. Paravan, S. Carlotti, L. Galfetti, Role of pressure and aluminum size in solid propellant CCP generation, AIAA Paper No. 2017-5076 (2017). doi:10.2514/6.2017-5076.

[33] R. Hermsen, Aluminum oxide particle size for solid rocket motor performance prediction, Journal of Spacecraft and Rockets 18 (6) (1981) pp. 483–490. doi:10.2514/3.57845.

[34] W. R. Cofer, III, E. Winstead, G. Purgold, R. Edahl, Solid propellant exhausted aluminum oxide and hydrogen chloride-environmental considerations, AIAA paper No. 1993-395 (1993). doi:10.2514/6.1993-305.

[35] D. Laredo, D. W. Netzer, The dominant effect of alumina on nearfield plume radiation, Journal of Quantitative Spectroscopy and Radiative Transfer 50 (5) (1993) pp. 511–530. doi:10.1016/0022-4073(93)90044-I.

[36] J. Traineau, P. Kuentzmann, M. Prévost, P. Tarrin, A. Delfour, Particle size distribution measurements in a subscale motor for the Ariane 5 solid rocket booster, AIAA Paper No. 1992-3049 (1992). doi:10.2514/6.1992-3049.

[37] D. Laredo, J. McCrorie, J. Vaughn, D. Netzer, Motor and plume particle size measurements in solid propellant micromotors, Journal of Propulsion and Power 10 (3) (1994) pp. 410–418. doi:10.2514/3.23750.

[38] W. D. Brennan, D. L. Hovland, D. W. Netzer, Measured particulate behavior in a subscale solid propellant rocket motor, Journal of Propulsion and Power 8 (5) (1992) pp. 954–960. doi:10.2514/3.23578.

[39] R. Dawbarn, M. Kinslow, D. J. Watson, Analysis of the measured effects of the principal exhaust effluents from solid rocket motors, Technical Report No. CR-3136, National Aeronautics and Space Administration (1980).

[40] R. A. Dobbins, L. D. Strand, A comparison of two methods of measuring particle size of Al2O3 produced by a small rocket motor, AIAA Journal 8 (9) (1970) pp. 1544–1550. doi:10.2514/3.5945.

[41] L. D. Strand, J. M. Bowyer, G. Varsi, E. G. Laue, R. Gauldin, Characterization of participates in the exhaust plume of large solid-propellant rockets, Journal of Spacecraft and Rockets 18 (4) (1981) pp. 297–305. doi:10.2514/3.57821.

[42] W. R. Cofer III, G. L. Pellett, D. I. Sebacher, N. T. Wakelyn, Surface chloride salt formation on Space Shuttle exhaust alumina, Journal of Geophysical Research: Atmospheres 89 (D2) (1984) pp. 2535–2540. doi:10.1029/JD089iD02p02535.

[43] W. R. Cofer III, G. G. Lala, J. P. Wightman, Analysis of mid-tropospheric Space Shuttle exhausted aluminum oxide particles, Atmospheric Environment (1967) 21 (5) (1987) pp. 1187–1196. doi:10.1016/0004-6981(87)90246-0.

[44] E. J. Beiting, Solid rocket motor exhaust model for alumina particles in the stratosphere, Journal of Spacecraft and Rockets 34 (3) (1997) pp. 303–310. doi:10.2514/2.3233.

[45] S. Gossé, L. Hespel, P. Gossart, A. Delfour, Morphological characterization and particle sizing of alumina particles in solid rocket motor, Journal of Propulsion and Power 22 (1) (2006) pp. 127–135. doi:10.2514/1.13626.

[46] W. Cofer III, G. Purgold, E. Winstead, R. Edahl, Space Shuttle exhausted aluminum oxide: A measured particle size distribution, Journal of Geophysical Research: Atmospheres 96 (D9) (1991) pp. 17371–17376. doi:10.1029/91JD01713.

[47] C. Hwang, G. Chang, Numerical study of gas-particle flow in a solid rocket nozzle, AIAA Journal 26 (6) (1988) pp. 682–689. doi:10.2514/3.9953.

[48] H.-O. Kim, D. Laredo, D. Netzer, Measurement of submicrometer Al2O3 particles in plumes, Applied optics 32 (33) (1993) pp. 6834–6840. doi:10.1364/AO.32.006834.

[49] K. M. Dill, R. A. Reed, V. S. Calia, R. J. Schulz, Analysis of crystalline phase aluminum oxide particles from solid propellant exhausts, Journal of Propulsion and Power 6 (5) (1990) pp. 668–671. doi:10.2514/3.23269.

[50] J. Shackelford, R. H. Doremus, Ceramic and glass materials: Structure, Properties and Processing, Chapter 1, 1st Edition, Springer, 2008.

[51] Anon, Malvern Mastersizer 2000 Operators Guide, MAN 0247, Issues 2.0, Malvern Instruments Ltd, Malvern, UK.

[52] Vertical Test Section Cologne (VMK) - Supersonic and Hypersonic Technology Department, German Aerospace Center DLR, URL: https://www.dlr.de/as/en/desktopdefault.aspx/tabid-194/407_read-5445/, Last Access: December 2020.

[53] D. Saile, D. Kirchheck, A. Gülhan, D. Banuti, Design of a hot plume interaction facility at DLR Cologne, in: Proceedings of the 8th European Symposium on Aerothermodynamics for Space Vehicles, 2015, Lisbon, Portugal.

[54] S. Carlotti, F. Maggi, A. Ferreri, L. Galfetti, R. Bisin, D. Saile, A. Gülhan, C. Groll, T. Langener, Development of an intrusive technique for particles collection in rockets plume, Acta Astronautica 158 (2019) pp. 361–374. doi:10.1016/j.actaastro.2018.06.030.

[55] S. Carlotti, F. Maggi, S. Dossi, R. Bisin, L. Galfetti, D. Saile, A. Gülhan, C. Groll, T. Langener, Overview of a supersonic probe for solid propellant rocket CCP collection, AIAA paper No. 2018-4882 (2018). doi:10.2514/6.2018-4882.

[56] F. Maggi, S. Carlotti, D. Saile, A. Guelhan, M. Liljedahl, N. Wingborg, T. Langener, J. Van Den Eynde, Experiments for collection and characterization of particles exiting from solid propellant rocket nozzles, AIAA paper No. 2020-3932doi:10.2514/6.2020-3932.

[57] F. E. Marble, Droplet agglomeration in rocket nozzles caused by particle slip and collision, Acta Astronautica 13 (2) (1967) 159–166.

[58] S. Gordon, B. McBride, Computer program for calculation of complex chemical equilibrium compositions and applications (1994).

[59] I. Glassman, R. F. Sawyer, The performance of chemical propellants, AGARDograph 129. Technivision Services, Slough, England (1970).